JACS
JOURNAL OF THE AMERICAN CHEMICAL SOCIETY
Article
Cite This: *J. Am. Chem. Soc.* 2019, 141, 11628−11640
pubs.acs.org/JACS

Thermodynamics and Electronic Properties of Heterometallic Multinuclear Actinide-Containing Metal−Organic Frameworks with "Structural Memory"

Otega A. Ejegbavwo,[†] Corey R. Martin,[†] Oyindamola A. Olorunfemi,[†] Gabrielle A. Leith,[†] Richard T. Ly,[†] Allison M. Rice,[†] Ekaterina A. Dolgopolova,[†] Mark D. Smith,[†] Stavros G. Karakalos,[‡] Nancy Birkner,[§,⊥] Brian A. Powell,[∥] Shubham Pandey,[▽] Robert J. Koch,[○] Scott T. Misture,[○] Hans-Conrad zur Loye,[†] Simon R. Phillpot,[▽] Kyle S. Brinkman,[§,⊥] and Natalia B. Shustova*,[†]

[†]Department of Chemistry and Biochemistry, University of South Carolina, Columbia, South Carolina 29208, United States
[‡]College of Engineering and Computing, University of South Carolina, Columbia, South Carolina 29208, United States
[§]Department of Materials Science and Engineering, Clemson University, Clemson, South Carolina 29634, United States
[∥]Department of Environmental Engineering and Earth Science, Clemson University, Clemson, South Carolina 29634, United States
[⊥]Center for Nuclear Environmental Engineering Sciences and Radioactive Waste Management (NEESRWM), Clemson University, Clemson, South Carolina 29634, United States
[▽]Department of Materials Science and Engineering, University of Florida, Gainesville, Florida 32611, United States
[○]Kazuo Inamori School of Ceramic Engineering, Alfred University, Alfred, New York 14802, United States

Supporting Information

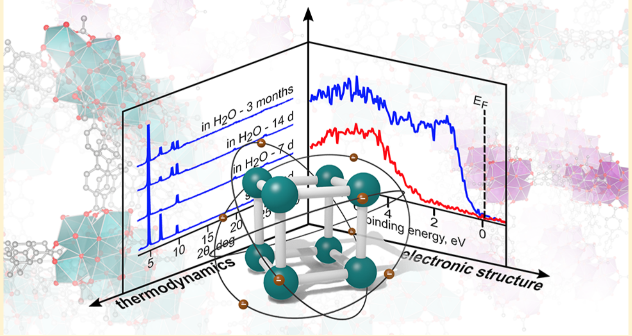

ABSTRACT: Thermodynamic studies of actinide-containing metal−organic frameworks (An-MOFs), reported herein for the first time, are a step toward addressing challenges related to effective nuclear waste administration. In addition to An-MOF thermochemistry, enthalpies of formation were determined for the organic linkers, 2,2′-dimethylbiphenyl-4,4′-dicarboxylic acid (H_2Me_2BPDC) and biphenyl-4,4′-dicarboxylic acid (H_2BPDC), which are commonly used building blocks for MOF preparation. The electronic structure of the first example of An-MOF with mixed-metal AnAn′-nodes was influenced through coordination of transition metals as shown by the density of states near the Fermi edge, changes in the Tauc plot, conductivity measurements, and theoretical calculations. The "structural memory" effect (i.e., solvent-directed crystalline−amorphous−crystalline structural dynamism) was demonstrated as a function of node coordination degree, which is the number of organic linkers per metal node. Remarkable three-month water stability was reported for Th-containing frameworks herein, and the mechanism is also considered for improvement of the behavior of a U-based framework in water. Mechanistic aspects of capping linker installation were highlighted through crystallographic characterization of the intermediate, and theoretical calculations of free energies of formation (ΔG_f) for U- and Th-MOFs with 10- and 12-coordinated secondary building units (SBUs) were performed to elucidate experimentally observed transformations during the installation processes. Overall, these results are the first thermochemical, electronic, and mechanistic insights for a relatively young class of actinide-containing frameworks.

INTRODUCTION

The stability of actinide-containing architectures and their chemical interactions with the environment have been increasingly studied over the past decades because of their significance for nuclear waste administration.[1−4] Due to their modularity, structural versatility, high porosity, and high tunability, metal−organic frameworks (MOFs)[5−9] have been utilized as a platform for nuclear waste sequestration[10] and actinide immobilization,[11] resulting in the development of materials[12] with a high actinide content and possessing minimal structural density.[13−21] However, the field of actinide-based MOFs,[22] especially in comparison with non-actinide-containing frameworks,[23−27] suffers from the fact that fundamental properties including thermodynamics, electronics, or detailed photophysics have not been investigated.

Herein, we report (i) the first thermochemical studies performed for any An-based MOFs including several examples

Received: May 2, 2019
Published: June 20, 2019

DOI: 10.1021/jacs.9b04737
J. Am. Chem. Soc. 2019, 141, 11628−11640

of the common organic linkers, (ii) the first example of heterometallic multinuclear An-MOF nodes with a coordinated transition metal and the first electronic structure studies using density of states (DOS) and conductivity measurements, (iii) over three-month water stability of a Th-MOF, (iv) structural "crystalline−amorphous−crystalline" cycling of An-MOFs as a function of metal node geometry, and (v) theoretical studies establishing the dependence of An-MOF stability on the nature of linker connectivity to the secondary building unit (SBU, Scheme 1). In addition, novel actinide-containing frameworks, M-Linker-*n*, (M (Th, U) = a metal in the node, Linker = an organic linker, and *n* = number of carboxylic groups attached to a metal node) such as $Th_6O_4(OH)_4(NO_3)_2(Me_2BPDC)_5$ (Th_6-Me_2BPDC-NO_3-10; Me_2BPDC^{2-} = 2,2′-dimethylbiphenyl-4,4′-dicarboxylate), $Th_6O_4(OH)_8(Me_2BPDC)_4$ (Th_6-Me_2BPDC-8), and $U_6O_4(OH)_4(TFA)_2(Me_2BPDC)_5$ (U_6-Me_2BPDC-TFA-10, TFA = trifluoroacetate, Figures 1 and S4), were prepared.

Scheme 1. Overview of the Presented Results: Thermodynamics, Electronic Structure, and "Structural Memory" Effect of An-MOFs

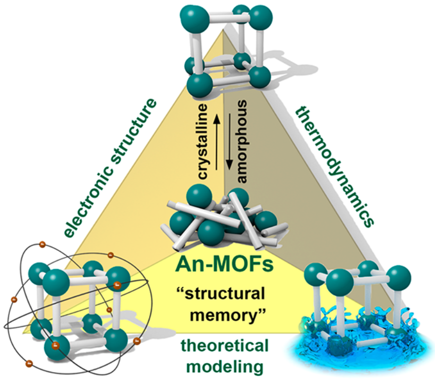

The discussion in this paper will be organized in the following order: synthetic details and chemical stability of the An-MOFs, their thermochemical studies including the measurements for organic linkers, analysis of the electronic structure of the heterometallic An-MOFs, "structural memory" effect of An-MOFs (i.e., solvent-directed crystalline−amorphous−crystalline cycling as a function of metal node geometry), and mechanistic insights on the capping linker installation process (i.e., postsynthetic linker coordination to framework metal nodes). The comprehensive analysis of An-MOFs includes single-crystal and powder X-ray diffraction (PXRD), inductively coupled plasma mass spectrometry (ICP-MS), conductivity, solution calorimetric measurements, thermogravimetric analysis, nuclear magnetic resonance (NMR), Fourier transform infrared (FTIR), and X-ray photoelectron spectroscopies (XPS), as well as theoretical modeling.

■ RESULTS AND DISCUSSION

Synthetic Details and Chemical Stability. Preparation of $Th_6O_4(OH)_4(NO_3)_2(Me_2BPDC)_5$ (Th_6-Me_2BPDC-NO_3-10), consisting of Th-metal nodes (Figures 1 and S4), has been performed solvothermally by heating $Th(NO_3)_4{\cdot}H_2O$ and H_2Me_2BPDC in *N*,*N*-dimethylformamide (DMF) at 120 °C for 24 h (Figure S4, more experimental details can be found in the Supporting Information (SI) and Experimental Section below). The presence of labile nitrate groups coordinated to the equatorial position of metal nodes allowed us to perform postsynthetic linker installation as described below (Figure 6). The $Th_6O_4(OH)_4(BPDC)_6(DMF)_6$ MOF (Th_6-BPDC-12; $BPDC^{2-}$ = biphenyl-4,4′-dicarboxylate) was prepared by heating $Th(NO_3)_4{\cdot}H_2O$ and H_2BPDC in DMF at 120 °C for 72 h.

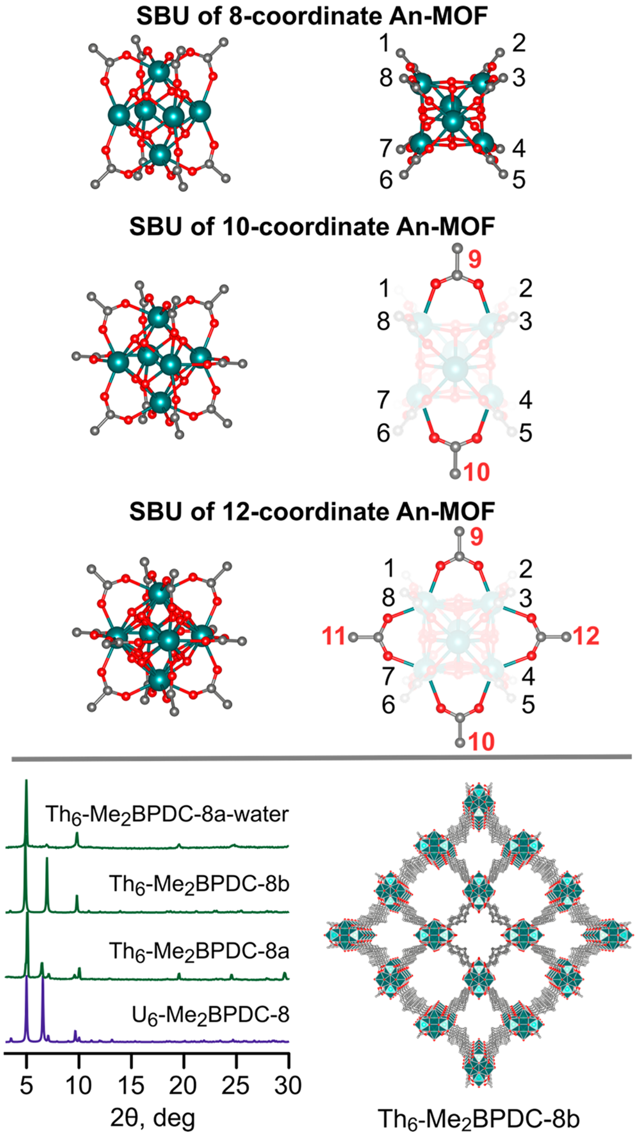

Figure 1. (*top*) Two views of secondary building units: 8-coordinated (*top*), 10-coordinated (*middle*), and 12-coordinated metal nodes (*bottom*). (*bottom, left*) PXRD patterns of U_6-Me_2BPDC-8 (simulated),[3] Th_6-Me_2BPDC-8a (experimental), Th_6-Me_2BPDC-8b (simulated), and Th_6-Me_2BPDC-8a in water (experimental). (*bottom, right*) X-ray crystal structure of Th_6-Me_2BPDC-8b. The teal, red, and gray spheres represent Th, O, and C atoms, respectively. Hydrogen atoms and solvents molecules were omitted for clarity.

Modification of the synthetic conditions by increasing the molar ratio of metal salt to linker used for Th_6-Me_2BPDC-NO_3-10 preparation allowed us to reduce the "metal-node-saturation degree" resulting in the synthesis of Th_6-Me_2BPDC-8 with eight linkers per metal node versus ten Me_2BPDC^{2-} observed for Th_6-Me_2BPDC-NO_3-10. Unsaturated nodes (i.e., with a number of linkers <12) can affect framework chemical stability[28] as discussed below. We were able to isolate two different phases of Th_6-Me_2BPDC-8: Th_6-Me_2BPDC-8a and Th_6-Me_2BPDC-8b. The Th_6-Me_2BPDC-8b MOF crystallizes in the tetragonal $P4_2/mmc$ space group ($a = b = 25.5223(17)$ Å and $c = 14.6275(11)$ Å), while Th_6-Me_2BPDC-8a is isostructural to previously reported U_6-Me_2BPDC-8,[3] ($P4_2/mmc$ space group) possessing $a = b = 24.9768(18)$ Å and $c = 15.9864(12)$ Å unit cell parameters. A phase transition from Th_6-Me_2BPDC-8a to Th_6-Me_2BPDC-8b was observed after soaking of Th_6-Me_2BPDC-8a in water, and then the reverse transformation from Th_6-Me_2BPDC-8b to Th_6- Me_2BPDC-8a was detected through reimmersion of Th_6-Me_2BPDC-8b into DMF (Figure S5). Since Th_6-Me_2BPDC-8a was isolated as the major pure phase, it has been chosen for further comprehensive analysis described below, and it will be referred to as “Th_6-Me_2BPDC-8” (without “a”) in the rest of the manuscript for simplicity.

As a first step to study the thermochemistry and electronic structure of An-MOFs, we explored their chemical stability. For instance, we observed significantly different behavior of Th-MOFs (Th_6-Me_2BPDC-8 or Th_6-Me_2BPDC-NO_3-10) versus U_6-Me_2BPDC-8, which could be partially explained by a wide range of accessible oxidation states in the latter case.

Crystals of Th_6-Me_2BPDC-8 were immersed in water, and changes in crystallinity were monitored by PXRD. We found that Th_6-Me_2BPDC-8 remained stable in water for three months, the longest time reported for any An-MOFs, rendering Th_6-Me_2BPDC-8 as one of the most water stable An-MOFs reported to date (Figure 2). Following this result, the stability of U_6-Me_2BPDC-8 was also explored. Crystals of U_6-Me_2BPDC-8 were soaked in water for a week under a nitrogen atmosphere. The uranium-based MOF retained its crystallinity under prolonged immersion in water, preserving uranium in the +4 oxidation state, a unique feature which was only achieved due to the fact that the framework was kept under an inert atmosphere. In air, U^{4+} transforms to U^{6+} based on XPS studies leading to framework degradation. In contrast, Th_6-Me_2BPDC-8 (Th has only one stable oxidation state, +4) does not require this specific precaution, and as expected, Th^{4+} was preserved in air. Under a nitrogen atmosphere, U_6-Me_2BPDC-8 not only retains its crystallinity, but the single crystals were still suitable for single-crystal X-ray diffraction analysis (Figure 2).

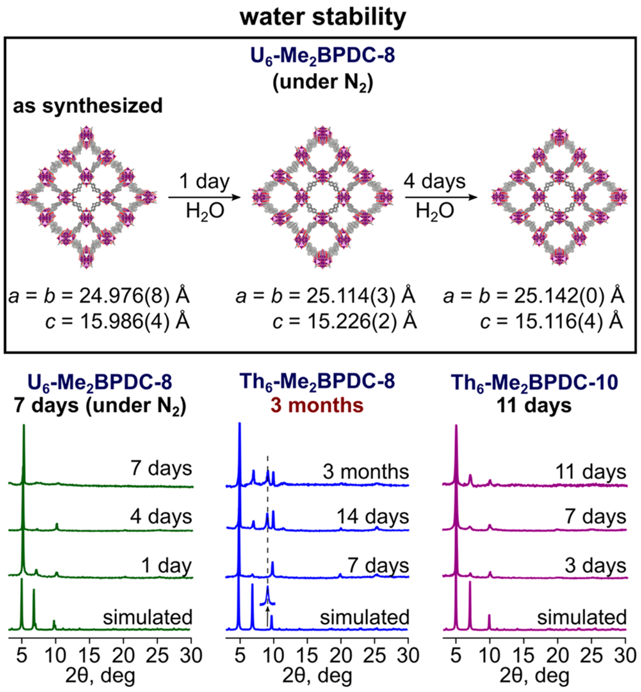

Figure 2. (*top*) X-ray crystal structures of U_6-Me_2BPDC-8: as-synthesized, after 1 day in water, and after 4 days in water. (*bottom, left*) PXRD patterns of U_6-Me_2BPDC-8: simulated, after 1 day in water, after 4 days in water, and after 7 days in water. (*bottom, middle*) PXRD patterns of Th_6-Me_2BPDC-8: simulated, after 7 days in water, after 14 days in water, and after three months in water. (*bottom, right*) PXRD patterns of Th_6-Me_2BPDC-NO_3-10 after 3, 7, and 11 days in water.

A crystallographic comparison between as-synthesized U_6-Me_2BPDC-8 and the same sample after immersion in water for 4 days revealed that the framework structure compressed along the c-axis ($\Delta = 0.87$ Å) and exhibited a slight elongation along the a and b axes ($\Delta = 0.17$ Å) resulting in an overall unit cell volume shrinkage ($\Delta = 417$ Å^3) from 9972 Å^3 to 9555 Å^3.

Prompted by the successful water stability experiments with the An-MOF-8, we proceeded to analyze the stability of An-MOFs with 10-coordinated SBUs, specifically Th_6-Me_2BPDC-NO_3-10. The same unexpected result was observed for Th_6-Me_2BPDC-NO_3-10, which was found to be stable in water for 11 days (Figure 2). The FTIR spectroscopic studies of the water-treated An-MOFs (Figures S9 and S10) confirmed the replacement of DMF with water in the MOFs through monitoring the gradual increase of the broad band corresponding to the ν(O−H) (3400 cm^{-1}) stretching mode of water, as well as the decrease of stretching modes corresponding to DMF molecules (2927 cm^{-1}, 1254 cm^{-1}, 1137 cm^{-1}, and 1090 cm^{-1}). To summarize, we demonstrated that An-MOFs, in particular, Th-containing frameworks can substantially surpass the previously reported limited stability and, in fact, can retain their structural integrity in aqueous environments for significant lengths of time.

The effect of a saturated metal node on An-MOFs was evaluated using a Th-based MOF with 12-coordinated SBUs (Th_6-BPDC-12).[29] This MOF, which is analogous to the very stable Zr-based MOF (UiO-67, UiO = University of Oslo),[30] was observed to also be extremely stable in water for at least one month (Figure S28). However, no reversible structural transformations were detected in this system, implying that MOF structural dynamism is a function of a metal-node saturation degree.[28]

After the water stability tests, we investigated the stability of the robust Th_6-Me_2BPDC-8 in air. The structural degradation and subsequent restoration of the crystallinity of the 8-coordinate Th-MOF in different solution environments were monitored by PXRD. When the Th_6-Me_2BPDC-8 is exposed to air, we observed significant framework degradation as shown in Figure 3. However, the crystallinity was restored after exposure to DMF for just 1 h, as shown in Figure 3. A similar tendency has previously been observed for Zr frameworks, which underwent significant structural transformations during framework evacuation, while a reverse structural process occurred upon immersion of the Zr-MOF in DMF.[19,31−33] Thus, we demonstrated, for the first time, that an actinide-containing MOF, Th_6-Me_2BPDC-8, possesses a great degree of flexibility by undergoing more drastic reversible phase transformations in comparison with the robust and “more conservative” Zr-MOF.[34]

Thermochemical Studies. Intrigued by the exceptional water stability of the An-MOFs, we delved into thermochem-

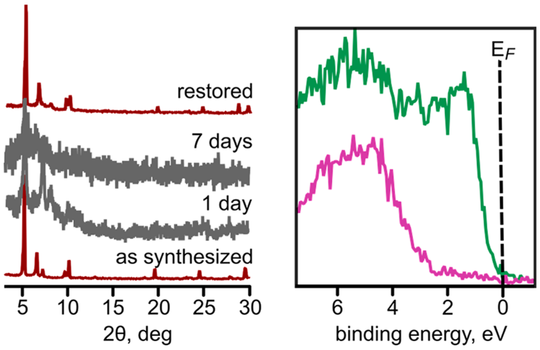

Figure 3. (*left*) PXRD patterns of Th_6-Me_2BPDC-8: as-synthesized (red), in air for 1 day (gray), in air for 7 days (gray), and restored in DMF for 1 h after prolonged exposure to air (red). (*right*) XPS data for the valence band region for $U_{1.23}Th_{4.77}Co_3$-Me_2BPDC-8 (U/Th-Co-8) (green) and $U_{1.23}Th_{4.77}$-Me_2BPDC-8 (U/Th-8) (purple).

ical studies to acquire fundamental knowledge that is not currently available for any actinide-based frameworks. However, this information is a cornerstone for future MOF phase development and possibly could shed light on the energetics of host−guest interactions inside such frameworks.[35−37] Specifically, we determined the enthalpies of dissolution (ΔH_s) and formation (ΔH_f) for two different linkers, $H_2MeBPDC$ and H_2BPDC, commonly used in the field of MOFs to ensure that such information can be used for further thermochemical MOF studies.

Due to the high stability described above, the Th_6-Me_2BPDC-8 framework was chosen for room temperature solution calorimetry measurements to determine the standard enthalpy of formation (ΔH_f°, Tables 1, S1, and S2). To perform this study, the sample was placed in a controlled atmosphere glovebox (0.2 ppm of O_2 and H_2O) loaded into glass ampules and subsequently sealed. The ampule was then transferred to a TAM III (TA Instruments) room temperature solution microcalorimeter and immersed in a 2:1 (v:v) 5 M HCl/DMF solvent system while recording changes in temperature offset values.[38] Thermochemical cycle reaction equations were employed to calculate the reaction dissolution enthalpy, and experimentally measured and related thermodynamic values were used to calculate the enthalpy of formation for Th_6-Me_2BPDC-8.

Table 1. Enthalpies of Formation of Th_6-Me_2BPDC-8 Evacuated and Nonevacuated, H_2Me_2BPDC, and H_2BPDC Computed from Experimental Thermodynamic Data[a]

	ΔH_s, kJ/mol	$\Delta H_{f,298\ K}$, kJ/mol
Th_6-Me_2BPDC-8	$-383.73^b \pm 7.75^c$	-14317.45 ± 8.6^d
Th_6-Me_2BPDC-8 (evacuated)	$-312.21^b \pm 6.53^c$	-9387.08 ± 7.72^e
ThO_2 (Thorianite)	$311.65 \pm 1.8^{e,40}$	-1226.4 ± 3.50^{41}
H_2Me_2BPDC	4.48 ± 0.06	-715.22^{39}
H_2BPDC	13.25 ± 0.06	-651.00^{39}
DMF	-9.45 ± 0.01	-239.4 ± 1.20^{42}
H_2O	0.07^{38}	-285.8 ± 0.10^{41}

[a] ΔH_s (*left*) and ΔH_f (*right*) are the enthalpies of dissolution and formation, respectively. [b] Average of the measurements. [c] The standard error of the average value. [d] Computed as the square root of the sum of squares of reported errors. [e] Computed for the solvent (2:1 v:v 5 M HCl/DMF, dissolution at pH = 3.3).

Standard enthalpies of formation from the elements, $\Delta H_f^\circ{}_{(298\ K)}$, for the Th-MOF sample were calculated using the appropriate standard enthalpies of formation of the reaction components multiplied by their reaction stoichiometric coefficients and including the dissolution reaction formation enthalpy of the sample. The data and computed results are reported in Tables 1, S1, and S2 as an average of the measurements with uncertainties reported as the standard error of the experimental average.[39−42] The average measured dissolution enthalpy for Th_6-Me_2BPDC-8 (as synthesized) was found to be −383.73 ± 7.75 kJ/mol per formula unit (see Table 1 and the Supporting Information for more details). The calculated enthalpy from solution components for Th_6-Me_2BPDC-8 is 2030.47 ± 7.96 kJ/mol of formula, which corresponds to 338.32 ± 1.33 kJ/mol enthalpy per mole of Th (more information on the equations is given in the SI). To shed more light on An-MOFs stability, we further estimated the stabilizing effect of the solvent (DMF) occupying the MOF pores.[45] To effectively perform this study, we carried out solution calorimetry on the evacuated sample of Th_6-Me_2BPDC-8. We found the measured dissolution enthalpy to be −312.21 ± 6.53 kJ/mol of formula unit. The calculated enthalpy from solution components for evacuated Th_6-Me_2BPDC-8 is 2148.90 ± 7.96 kJ/mol of formula, which corresponds to 360.10 ± 1.13 kJ/mol enthalpy per mole of Th, implying that the DMF solvent stabilizes Th_6-Me_2BPDC-8 by −21.78 ± 1.33 kJ/mol per mole of Th. These observations show that DMF solvent is more stabilizing in the Th-MOF in comparison with the stabilization effects of solvent reported for MOF-5 (−4.8 kJ/mol of Zn)[43] and ZIF-4 (−3.0 kJ/mol of Zn).[46] The standard heat of formation of the evacuated Th-MOF from its components in their standard state was also computed to be −9387.08 ± 7.72 kJ/mol (Table 1). The results obtained from our studies show that the solvent molecules contribute to the stabilization of the Th_6-Me_2BPDC-8 MOF, suggesting a strong interaction of the solvent with the MOF. This solvent−framework interaction is therefore suggested as a key to the observed “structural memory” effect exhibited by the Th-MOF. Following this experiment, the standard heat of formation of the Th-MOF from its components in their standard state was also computed. The obtained value for Th_6-Me_2BPDC-8 (Table 1) was found to be −14317.45 ± 8.60 kJ/mol. Thus, according to the determined values, MOF formation is a favorable process which is in line with the previous observations made for $Cu_3(BTC)_2$ (BTC^{3-} = benzenetricarboxylate), $Zn_3(BTC)_2$, and MOF-5.[38,43,44]

Electronic Structure of Heterometallic An-MOFs. The tunability of the electronic properties of An-MOFs is an unexplored challenge but, at the same time, a fascinating opportunity to compare the effect of *f*-electrons and unusual oxidation states on the electronic structure of a framework. In this manuscript, we compare the electronic properties of the parent An-MOFs with the properties of heterometallic AnAn′-MOF and AnAn′M-MOF (M = transition metal).

As a method to synthesize AnAn′-MOFs, we have chosen postsynthetic cation exchange, in which U_6-Me_2BPDC-8 crystals were soaked in a solution of $ThCl_4$, resulting in the formation of $U_{1.23}Th_{4.77}$-Me_2BPDC-8. The ratio of uranium to thorium was determined by ICP-MS. As a result of this transformation, the dark green powder converts to an almost white sample. Interestingly, such transmetalation did not occur under a nitrogen atmosphere but only when performed in air. The U_6-Me_2BPDC-8 framework remained intact, and reaction progress was only notable after exposure of the reaction mixture to air. This fact could be explained if the driving force for transmetalation relies on the formation of a stable UO_2^{2+} fragment accompanied by changes in the oxidation state of uranium from +4 to +6. This fact is in line with our findings, which demonstrate that U-MOFs are not stable in air (only under a nitrogen atmosphere) in contrast to very robust Th analogs.

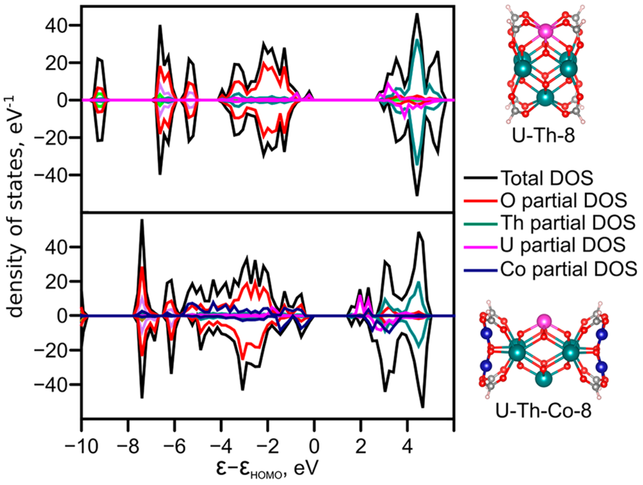

Figure 4. (*left*) Total and partial density of states (DOS) and (*right*) truncated models calculated using the GGA-PBE level of theory and DFT+*U* corrections on U (*f*-electrons) and Co (*d*-electrons): (*top*) $U_{1.23}Th_{4.77}$-Me_2BPDC-8 and (*bottom*) $U_{1.23}Th_{4.77}Co_3$-Me_2BPDC-8. The green, lilac, red, gray, and dark blue spheres represent Th, U, O, C, and Co atoms, respectively.

One of the requirements for coordination of a transition metal to An-metal nodes is the presence of unsaturated metal nodes. Therefore, we have chosen the stable $U_{1.23}Th_{4.77}$-Me_2BPDC-8 possessing vacant sites for transition metal coordination (Figure 4). The $U_{1.23}Th_{4.77}$-Me_2BPDC-8 framework was heated in a 0.25 M $Co(NO_3)_2$ solution at 75 °C for 48 h, resulting in $U_{1.23}Th_{4.77}Co_3$-Me_2BPDC-8. Cobalt was chosen as a transition metal due to the intriguing behavior previously observed for other cobalt-containing heterometallic MOFs.[47,48] Attempts at incorporation of Co(II) directly into the U_6-Me_2BPDC-8 MOF were unsuccessful due to instability of the U-MOF. Initially, we employed XPS analysis of $U_{1.23}Th_{4.77}$-Me_2BPDC-8 and $U_{1.23}Th_{4.77}Co_3$-Me_2BPDC-8 MOFs to monitor changes in the DOS near the Fermi edge (E_F) upon incorporation of the cobalt ion (Figure 3).

Through comparison of the band gap values estimated from Tauc plots (Figure S14), we observed a decrease of the band gap from 3.3 eV (Th_6-Me_2BPDC-8) to 2.5 eV ($U_{1.23}Th_{4.77}$-Me_2BPDC-8) in the case of An-MOF comprised of both uranium and thorium. The integration of cobalt into $U_{1.23}Th_{4.77}$-Me_2BPDC-8 led to further band gap reduction to 1.9 eV.

To rationalize such changes in the electronic structures of heterometallic An-MOFs, we carried out theoretical studies on the truncated model of the $U_{1.23}Th_{4.77}$-Me_2BPDC-8 (U/Th-8, Figure 4) and $U_{1.23}Th_{4.77}Co_3$-Me_2BPDC-8 (U/Th-Co-8, Figure 4) MOFs. The density functional theory (DFT) calculations revealed that the Co node extension in $U_{1.23}Th_{4.77}$-Me_2BPDC-8 (Figure 4) resulted in changes of the electronic structure near E_F. The band gap values for $U_{1.23}Th_{4.77}$-Me_2BPDC-8 and $U_{1.23}Th_{4.77}Co_3$-Me_2BPDC-8 were found to be 3.0 and 1.9 eV, respectively. The partial DOS shown in Figure 4 were obtained by adding the atomic projected DOS over different groups of elements such as C, H, O, Th, U, and Co. Although these plots include contribution from all orbitals, the orbital-projected DOS suggest that DOS of $U_{1.23}Th_{4.77}$-Me_2BPDC-8 near E_F originate mainly from the uranium 5*f*-orbitals, whereas the DOS above E_F (conduction band) are primarily composed of U and Th 5*f*-orbitals (Figure 4). When the metal nodes are extended by cobalt, the DOS near E_F are dominated by contributions from the Co 3*d*-orbitals and oxygen 2*p*-orbitals (Figure 4), and the band gap is reduced to 1.9 eV. As expected, the decrease of the band gap resulted in changes of the electronic properties of heterometallic MOFs. Indeed, the conductivity (σ) of $U_{1.23}Th_{4.77}$-Me_2BPDC-8 was found to be 7.0×10^{-10} S·cm^{-1}, and it was enhanced by 3 orders of magnitude in the case of cobalt incorporation to 1.4×10^{-7} S·cm^{-1} (for $U_{1.23}Th_{4.77}Co_3$-Me_2BPDC-8). Our current studies represent the initial steps for achieving improved understanding of the behavior of heterometallic systems containing two or more atoms and can possibly lead to the ability to tune the electronic structure of An-MOFs.

"Structural Memory" Effect of An-MOF. There are a number of studies revealing the unprecedented stability of Zr-based frameworks.[28,49,50] For instance, it was reported that the Zr-based MOF (UiO-67)[30] with 12-coordinated SBUs is stable in a wide range of solvents for an extended period of time without detectable structural changes.[51] Indeed, our studies of Zr_6-Me_2BPDC-8[52] in a range of solvents, including methanol (MeOH), ethanol (EtOH), acetonitrile (ACN), hexanes, dichloromethane (DCM), chloroform, ethyl acetate (EtOAc), and tetrahydrofuran (THF), demonstrate that the structural integrity was preserved, and in addition, there were no or only minimal structural transformations observed as shown in Figures 5 and S26. In contrast, our study of the relatively robust Th_6-Me_2BPDC-8 framework, possessing the same metal node arrangement as its Zr-analog,[52] revealed structural dynamism (i.e., breaking a long-range structural order resulting in a significant loss of MOF crystallinity and its restoration as a function of exposure to solvent (Figures 5 and S22−26)).

We studied structural dynamism in Th_6-Me_2BPDC-8 and Th_6-Me_2BPDC-NO_3-10 MOFs using 11 different solvents (ranging from polar protic and polar aprotic to nonpolar solvents). Exposure of Th_6-Me_2BPDC-8 to solvents such as MeOH and ACN resulted in significant loss of crystallinity (Figures 5 and S23). However, MOF crystallinity was fully restored by soaking the relatively amorphous samples in DMF, *N*,*N*-diethylformamide, or *N*,*N*-dimethylacetamide (Figure S21). In other polar protic solvents such as EtOH or aprotic solvents such as THF, EtOAc, acetone, or ACN, the PXRD revealed similar crystallinity loss except for Th_6-Me_2BPDC-NO_3-10 in MeOH. This fact allowed us to closely look into the transformation of Th_6-Me_2BPDC-NO_3-10 in methanol using single-crystal X-ray diffraction since the crystals were preserved upon solvent exchange. Despite the fact that the data collection was performed on Th_6-Me_2BPDC-NO_3-10 crystals sealed in a capillary under solvent (Figure S19), the structural analysis revealed changes in the unit cell parameters from $a = b = 23.7918(8)$ Å and $c = 19.6923(7)$ Å for pristine Th_6-Me_2BPDC-NO_3-10 (see the SI) to $a = b = 24.0205(8)$ Å and $c = 19.7574(6)$ Å observed for the Th-MOF immersed into methanol. As shown in a recent comprehensive literature

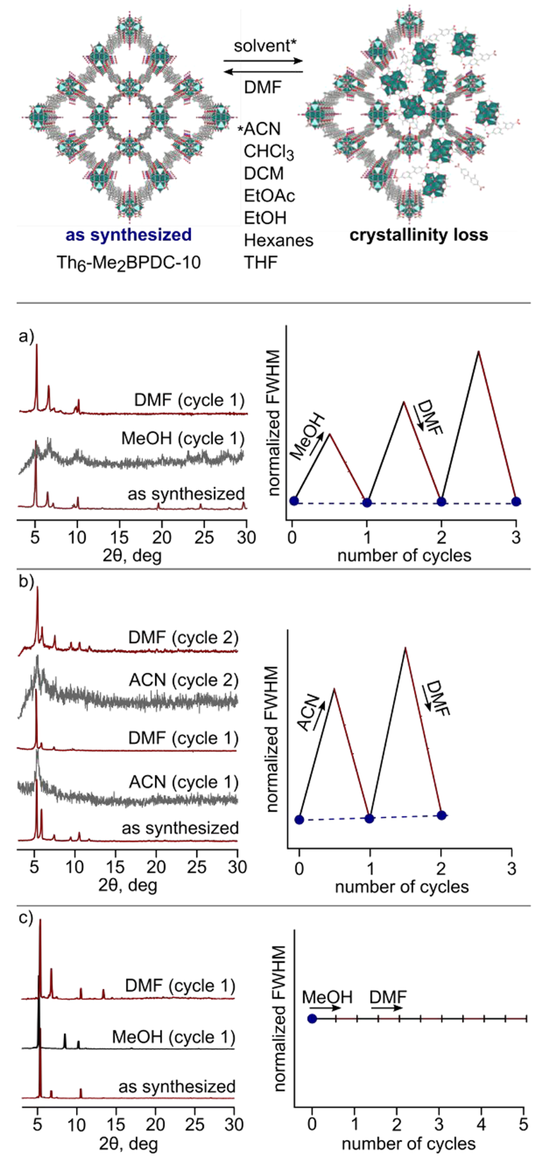

Figure 5. (*top*) Schematic representation of the crystallinity loss observed for Th$_6$-Me$_2$-BPDC-NO$_3$-10 in the listed solvents and the restoration of the framework in DMF. (*a*) PXRD patterns of Th$_6$-Me$_2$BPDC-8: as-synthesized, in methanol, and in DMF. (*b*) PXRD patterns of Th$_6$-Me$_2$BPDC-NO$_3$-10: as-synthesized, in acetonitrile, and in DMF. "Crystalline−amorphous−crystalline" cycling was performed as a function of changes in a full width at half-maximum (FWHM) measured for the (110) reflection peak. (*c*) PXRD patterns of Zr-Me$_2$BPDC-8: as synthesized, in methanol, and in DMF.

analysis,[53] these structural crystalline-to-amorphous-to-crystalline changes are relatively rare even for MOFs constructed from transition metals,[53] and there have been no reports for any type of An-containing framework. In addition to studying the solvation effect on structural reorganization, we probed the possibility of "structural cycling" (i.e., a series of crystalline−amorphous−crystalline transformations using alternation of "good" (DMF) and "bad" (MeOH or ACN) solvents). Figures 5 and S20 demonstrate that Th$_6$-Me$_2$BPDC-8 can undergo more than three cycles of crystallinity restoration in contrast to Th$_6$-Me$_2$BPDC-NO$_3$-10, for which only two such cycles were possible. As a control experiment, we performed similar studies using the stable Zr-analog (Zr$_6$-Me$_2$BPDC-8, PCN-700).[52] As expected, there was no evidence of structural dynamism, and PCN-700 did not undergo any structural transformations as shown in Figures 5 and S26. It is important to highlight that it is not a "breathing" behavior, a commonly known process for MOFs occurring during their evacuation, but rather a different concept: a "structural memory" effect (i.e., solvent-directed crystalline−amorphous−crystalline cycling as a function of metal node geometry), which is reported for the first time for actinide-containing frameworks.

Mechanistic Insights on Capping Linker Installation in An-MOFs. Reports by Yaghi and co-workers, Zhou and co-workers, and a number of other research groups have demonstrated the possibility of the functionalization of MOFs by postsynthetic installation of more than one capping linker.[52,54−59] Herein we report not only access to structures through sequential linker installation in Th-based MOFs, which could not be prepared by direct synthesis, but more importantly, through single-crystal X-ray studies, we elucidate a possible mechanism involved in the installation process. As in the case of transition metal coordination (described above), the main requirement for capping linker installation is the presence of unsaturated metal nodes. The Th$_6$-Me$_2$BPDC-NO$_3$-10 MOF meets the structural criteria (Figures 1 and S4) through the presence of unsaturated metal nodes, and the pocket **B** of 15.1 Å size (a distance between the centroids of the oxygen atoms of the terminal nitrate groups, Figure 6) is suitable for capping linker installation. This pocket size is in line with the 15.3 Å length of the linker 2,2″-dimethylterphenyl-4,4″-dicarboxylic acid (H$_2$Me$_2$TPDC, Figure 6). To perform installation, the crystals of Th$_6$-Me$_2$BPDC-NO$_3$-10 were heated in a DMF solution of H$_2$Me$_2$TPDC. The single-crystal X-ray diffraction analysis surprisingly revealed that instead of capping linker installation, heating of Th$_6$-Me$_2$BPDC-NO$_3$-10 for 24 h in a solution of H$_2$Me$_2$TPDC linker resulted in the formation of Th$_6$-Me$_2$BPDC-8, implying the detachment of two equatorial linkers, Me$_2$BPDC^{2-}, as shown in Figure 6.

In the intermediate with eight-coordinated SBUs, the linker removal resulted in the formation of a second pocket **A** with a size of 10.7 Å (a distance between the two centroids of the terminal oxygen atoms, Figure 6). Based on this data, it is plausible to suggest that linker installation could result in structural deformation of the MOF with 10-coordinated metal nodes to match the differences of the size of the Me$_2$BPDC linker and pocket **A** (Δd = 0.4 Å). For that transformation, the size of the other pocket **B** should be compressed, which is accompanied by the formation of the intermediate with vacant **A** and **B** pockets (Figure 6).

Focusing on the Th-MOF with the 8-coordinated SBUs as a possible intermediate in the installation process, we continued to explore the flexibility of the framework by attempting to reinstall the detached Me$_2$BPDC^{2-} linker. For that, the intermediate MOF was heated in a DMF solution of H$_2$Me$_2$BPDC and H$_2$Me$_2$TPDC for 2 days at 75 °C. The single-crystal X-ray data demonstrated installation of both linkers in **A** and **B** pockets resulting in the formation of 12-coordinated metal nodes. As shown in Figure 6, the size of pocket **B** expanded from 15.1 to 15.3 Å in order to accommodate the 15.3 Å-long Me$_2$TPDC^{2-} linker. To provide further mechanistic insights on capping linker installation occurring in An-containing frameworks, we explored installation of a linker with one phenyl ring (H$_2$BDC = 1,4-benzenedicarboxylic acid; length (l) = 6.9 Å), two phenyl rings

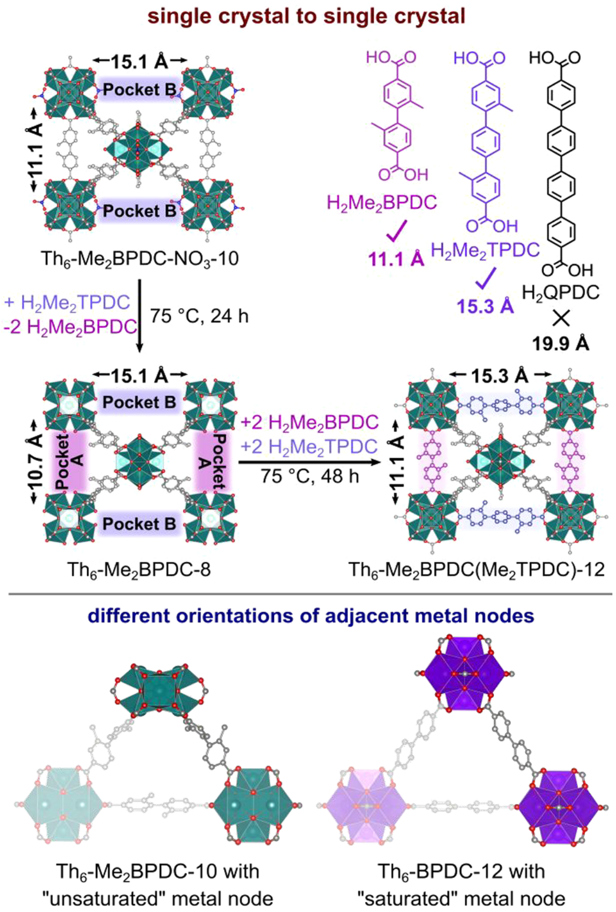

Energies of formation of M-10 and M-12 compounds from M-8 (M = Th, U).

system*	reaction	free energy, kJ/mol
U-10	U-8 + $2CO_2H_2 \rightarrow$ U-10	−308.372
U-12	U-8 + $4CO_2H_2 \rightarrow$ U-12	−640.880
Th-10	Th-8 + $2CO_2H_2 \rightarrow$ Th-10	−317.770
Th-12	Th-8 + $4CO_2H_2 \rightarrow$ Th-12	−688.606

Figure 6. (*top*) Schematic representation of the synthetic route for preparation of Th$_6$-Me$_2$BPDC(Me$_2$TPDC)-12 based on sequential linker installation using Th$_6$-Me$_2$BPDC-NO$_3$-10 as a precursor. (*middle*) Single-crystal X-ray structures of the 10-coordinate Th$_6$-Me$_2$BPDC-10 (*left*) and 12-coordinate Th$_6$-BPDC-12 (*right*) obtained via direct synthesis, highlighting the structural difference between the adjacent metal nodes of both MOFs. The teal and purple spheres were chosen for Th atoms for MOFs with 10- and 12-coordinated SBUs, respectively, while gray and red spheres represent C and O atoms. (*bottom*) Table of calculated energy of formation of the truncated 10 and 12 coordinated SBUs from the truncated model with the 8-coordinated SBU.

(H$_2$Me$_2$BPDC; l = 11.1 Å), and four phenyl rings (H$_2$QPDC = 1,1′,4′,1″,4″,1‴-quarterphenyl-4,4‴-dicarboxylic acid; l = 19.9 Å). The installation of the H$_2$BDC linker resulted in a change in the PXRD powder pattern (Figure S31) similar to observations by the Zhou group involving coordination of the same H$_2$BDC to a MOF with 8-coordinated Zr-nodes.[52] Figure S31 shows similarity in the PXRD pattern between the Th- and Zr-BDC-installed MOFs, indicative of successful installation of the BDC^{2-} linker into the Th$_6$-Me$_2$BPDC-NO$_3$-10 MOF. ^{1}H NMR spectroscopic studies of the digested MOF samples were further used to confirm installation of the BDC^{2-} linker into the MOF (Figure S35). Table S9 summarizes all installation attempts and the degree of capping linker integration. The installation processes of H$_2$Me$_2$BPDC and H$_2$QPDC into Th$_6$-Me$_2$BPDC-NO$_3$-10 were monitored via single-crystal X-ray diffraction and NMR/FTIR spectroscopy. In both cases, our attempts to facilitate the conversion from 10-to-12-coordinated metal nodes were unsuccessful. PXRD and single-crystal X-ray studies did not reveal any structural changes even after several days of heating of the parent framework in a solution of the corresponding linker. It is plausible to suggest that the linker with four phenyl rings (QPDC^{2-}) cannot fit due to its size (19.9 Å). However, the length of the Me$_2$BPDC^{2-} linker is more likely to fit into pocket **B** (l = 11.1 Å). To elucidate the possible reason impeding Th$_6$-Me$_2$BPDC-NO$_3$-10 to Th$_6$-Me$_2$BPDC-12 transformation, we attempted a 10-to-12 transformation using a nonmethylated H$_2$BPDC linker. Instead of a 10-to-12 transformation, the BPDC^{2-} replaced Me$_2$BPDC^{2-} as confirmed by single-crystal X-ray studies (Figure 7) resulting in a 10-coordinate Th$_6$-BPDC-10 MOF, which cannot be synthesized via direct synthesis. Furthermore, we prepared Th$_6$-BPDC-12 via direct synthesis. As shown in Figure 6, the orientation of adjacent metal nodes in Th$_6$-Me$_2$BPDC-10 does not allow for capping linker installation with the H$_2$MeBPDC linker (Figure S33) and is drastically different from that in Th$_6$-BPDC-12.

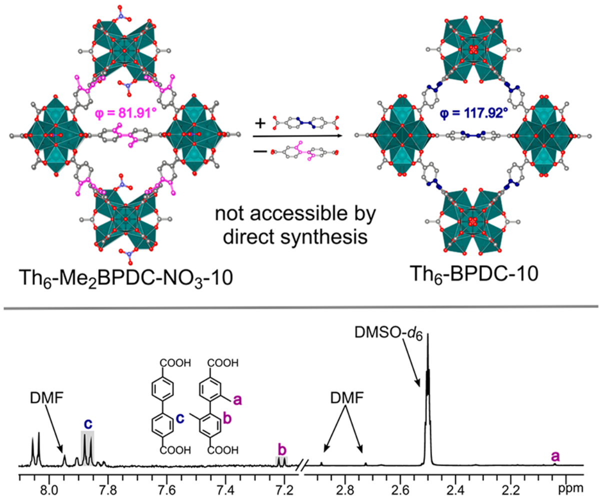

Figure 7. (*top*) Single-crystal-to-single-crystal linker replacement of Me$_2$BPDC^{2-} with BPDC^{2-} in Th$_6$-Me$_2$BPDC-NO$_3$-10. The Th$_6$-BPDC-10 MOF with the 10-coordinated SBUs cannot be achieved via direct synthesis. The teal, gray, red, and blue spheres represent Th, C, O, and N atoms, respectively. The H atoms were omitted for clarity. The dihedral angle in the Me$_2$BPDC^{2-} with BPDC^{2-} linkers are highlighted in pink and blue, respectively.

To elucidate the experimentally observed flexibility of the An-MOF systems, we carried out theoretical calculations to support the observed transformations during the installation processes.[60] Free energies of formation (ΔG_f) for the U- and Th-MOFs with 10-coordinated and 12-coordinated SBUs were calculated using their respective MOFs with 8-coordinated SBUs as reference structures. For such calculations, we employed the truncated cluster models, in which two formic acid linkers attached to a M-8 cluster resulting in a M-10 cluster and addition of four linkers results in a M-12 cluster

(Figure S2). The ΔG_f values were calculated using eqs (1) and (2) for M-10 and M-12, respectively.

$$\Delta G_f\{\text{M-10}\} = G_{\text{M-10}} - (G_{\text{M-8}} + 2G_{\text{HCOOH}}) \quad (1)$$

$$\Delta G_f\{\text{M-12}\} = G_{\text{M-12}} - (G_{\text{M-8}} + 4G_{\text{HCOOH}}) \quad (2)$$

We found that ΔG_f values for both M-10 and M-12 compounds are negative (Figure 6), thus confirming the experimental feasibility of the formation of MOFs with 10-coordinated and 12-coordinated SBUs from their analogs with 8-coordinated metal nodes.

■ CONCLUSION

The first studies of thermochemistry and electronic structure shed light on the properties of monometallic and heterometallic An-containing frameworks including the first examples of actinide-containing MOFs with incorporated transition metals. The thermochemical values reported for frameworks and organic linkers render the presented studies valuable for the future prediction of thermodynamic stability of frameworks. The An-MOFs with mixed-metal nodes allowed us to probe the effect of *f*-electrons on the electronic structure including the evaluation of the contribution from the transition metal. In combination with theoretical modeling, the electronic properties of An-MOFs were studied spectroscopically (i.e., DOS near the E_F and Tauc plots) and through conductivity measurements. The three-month water stability of An-MOFs provides an opportunity for their detailed studies even in aqueous media. The "structural memory" effect makes the considered framework containing a metal in the +4 oxidation state distinct from the widely used Zr(IV) analogs. We experimentally observed structural flexibility and dynamism of the Th-MOFs involving crystalline-to-amorphous-to-crystalline transformations upon solvent treatments.[61,62] Through single-crystal X-ray diffraction, we demonstrated that capping linker installation went through a unique intermediate, which has never been detected for any framework to date. In light of the extreme importance of proper radioactive waste administration, we envision that our studies are the first steps in attaining insights for utilizing An-based MOFs as a unique platform where chemical interactions between actinide-containing species can be fundamentally understood and expanded upon.

■ EXPERIMENTAL SECTION

Caution! Uranium and thorium salts are radioactive and chemically toxic reactants; suitable precautions, care, and protection for the handling of such substances must be followed.

Materials. UCl_4 (>95%, International Bio-Analytical Industries Inc.), $ThCl_4$ (>95%, International Bio-Analytical Industries Inc.), $Th(NO_3)_4 \cdot H_2O$ (99.8%, Strem Chemicals Inc.), $ZrCl_4$ (99.5%, Alfa Aesar), $Co(NO_3)_2 \cdot 6H_2O$ (99%, Strem Chemicals Inc.), potassium acetate (lab grade, Ward's Science), K_2CO_3 (lab grade, Ward's Science), 1,4-dibromobenzene (98%, Sigma-Aldrich), 4-methoxycarbonylphenylboronic acid (>97%, Boronic Molecular), 1,4-benzenedicarboxylic acid (99%, TCI chemicals), biphenyl-4,4′-dicarboxylic acid (97%, Oakwood Chemical), $Pd(PPh_3)_4$ (96%, Matrix Scientific), methyl-(4-iodo-3)-methylbenzoate (98%, BeanTown Chemical), 4,4′-diiodobiphenyl (98%, Matrix Scientific), 4,4,4′,4′,5,5,5′,5′-octamethyl-2,2′-bi-(1,3,2-dioxaborolane) (>98%, Ark Pharm), $PdCl_2(PPh_3)_2$ (96%, Oakwood Chemical), CsF (99%, Oakwood Chemical), KOH (ACS grade, Fisher Chemical), 2,5-dibromoaniline (97%, Oakwood Chemical), $Pd(OAc)_2$ (>95%, Ox-Chem), trifluoroacetic acid (99%, Sigma-Aldrich), nitric acid (70%, Sigma-Aldrich), tetrahydrofuran (ACS grade, Macron Fine Chemicals), dichloromethane (ACS grade, Oakwood Chemical), methanol (ACS grade, Fischer Scientific), ethanol (200 proof, Decon Laboratories, Inc.), hexanes (ACS grade, VWR Chemicals), dimethyl sulfoxide (ACS grade, Fisher Scientific), acetone (ACS grade, VWR Chemicals), acetonitrile (ACS grade, Fischer Scientific), chloroform (ACS grade, BDH), ethyl acetate (ACS grade, Fisher Scientific), *N,N*-dimethylacetamide (99%, Alfa Aesar), *N,N*-diethylformamide (99%, TCI chemicals), *N,N*-dimethylformamide (ACS grade, BDH), chloroform-*d* (Cambridge Isotope Laboratories, Inc.), and DMSO-d_6 (Cambridge Isotope Laboratories, Inc.) were used as received.

Synthesis. The compounds 1,4-benzenedicarboxylic acid (H_2BDC) and 4,4′-biphenyldicarboxylic acid (H_2BPDC) were commercially available while 2,2′-dimethylbiphenyl-4,4′-dicarboxylic acid (H_2Me_2BPDC),[63] 2,2″-dimethylterphenyl-4,4″-dicarboxylic acid (H_2Me_2TPDC),[64] quaterphenyl-4,4‴-dicarboxylic acid (H_2QPDC),[65] Zr_6-Me_2BPDC-8,[52] and U_6-Me_2BPDC-8[3] were prepared according to the reported procedures.

Synthesis and Characterization of Th_6-Me_2BPDC-NO_3-10. A mixture of $Th(NO_3)_4 \cdot H_2O$ (9.6 mg, 20 μmol), H_2Me_2BPDC (4.3 mg, 16 μmol), concentrated nitric acid (35 μL), and DMF (0.79 mL) was put in a 1-dram vial and heated in an isothermal oven at 120 °C for 24 h. After cooling to room temperature, the colorless crystals of Th_6-Me_2BPDC-NO_3-10 (7.2 mg, 2.3 μmol, yield: 73%) were collected by filtration and washed three times with DMF. FTIR (neat, cm^{-1}): 3438, 2927, 2864, 1656, 1593, 1537, 1408, 1383, 1255, 1207, 1093, 1062, 1007, 910, 863, 777, and 732 (Figure S6). The obtained crystals were suitable for single-crystal X-ray analysis. A detailed description of the data collection and refinement details is given in the Supporting Information. Table S3 contains the crystallographic refinement data. As shown in Figure S6, the PXRD pattern of as-synthesized Th_6-Me_2BPDC-NO_3-10 matches the simulated pattern from the single-crystal X-ray data. PXRD studies were also used to confirm the crystallinity of the bulk material (Figure S6). The thermal stability of Th_6-Me_2BPDC-NO_3-10 was studied by thermogravimetric analysis, which demonstrated rapid loss of solvent molecules at the 25−200 °C temperature range (Figure S12). The observed weight loss (~40 wt %) at this temperature range can be attributed to removal of the noncoordinated solvent mixture of DMF and H_2O.

Synthesis and Characterization of Th_6-Me_2BPDC-8. A mixture of $Th(NO_3)_4 \cdot H_2O$ (31 mg, 64 μmol), H_2Me_2BPDC (4.3 mg, 16 μmol), nitric acid (25 μL), and DMF (0.75 mL) was put in a 1-dram vial and heated in an isothermal oven at 120 °C for 24 h. After cooling to room temperature, the colorless crystals of Th_6-Me_2BPDC-8a (8.1 mg, 2.9 μmol, yield: 74%) were collected by filtration and washed three times with DMF. IR (neat, cm^{-1}): 3418, 2930, 2860, 1650, 1587, 1543, 1466, 1408, 1382, 1297, 1254, 1207, 1137, 1094, 1062, 1032 1007, 912, 863, 815, 778, 734, and 660 (Figure S7). A prolonged 72 h heating of the mixture resulted in Th_6-Me_2BPDC-8b (minor phase) crystals which were suitable for single-crystal X-ray analysis. A detailed description of the data collection and refinement details is given in the Supporting Information. Table S3 contains the crystallographic refinement data. As shown in Figure S7, the PXRD pattern of as synthesized Th_6-Me_2BPDC-8a matches the simulated pattern from the single-crystal X-ray data for U_6-Me_2BPDC-8. PXRD studies were also used to confirm the crystallinity of the bulk material (Figure S7). The thermal stability of Th_6-Me_2BPDC-8a was studied by thermogravimetric analysis, which demonstrated rapid loss of solvent molecules at the 25−175 °C temperature range (Figure S11). The observed weight loss (~37 wt %) at this temperature range can be attributed to removal of the noncoordinated solvent mixture of DMF and H_2O.

Synthesis and Characterization of Th_6-BPDC-12. A mixture of $Th(NO_3)_4 \cdot H_2O$ (12 mg, 26 μmol), H_2BPDC (1.6 mg, 6.4 μmol), trifluoroacetic acid (25 μL), and DMF (0.56 mL) was put in a 1-dram vial and heated in an isothermal oven at 120 °C for 72 h. After cooling to room temperature, the colorless crystals of Th_6-BPDC-12 (2.5 mg, 0.70 μmol, yield: 69%) were collected by filtration and washed three times with DMF. IR (neat, cm^{-1}): 3339, 2932, 1651, 1591, 1535, 1497, 1388, 1254, 1201, 1178, 1145, 1098, 1062, 1020, 1006, 855, 838, 796, 769, 702, 672, and 662 (Figure S28). The obtained crystals

DOI: 10.1021/jacs.9b04737
J. Am. Chem. Soc. 2019, 141, 11628−11640

were suitable for single-crystal X-ray analysis. The single-crystal structure (Figure S27) and a detailed description of the data collection and refinement details are given in the Supporting Information. As shown in Figure S28, the PXRD pattern of as-synthesized Th_6-BPDC-12 matches the simulated pattern from the single-crystal X-ray data. PXRD studies were also used to confirm the crystallinity of the bulk material (Figure S28). The thermal stability of Th_6-BPDC-12 was determined via thermogravimetric analysis (Figure S12).

Preparation of U_6-Me_2BPDC-8-H_2O-1d and U_6Me_2BPDC-8-H_2O-4d. The green crystals of U_6-Me_2BPDC-8 were washed once with DMF and soaked in water for 1 or 4 days at room temperature under an inert atmosphere. Detailed description of the data collection and refinement details is given in the Supporting Information. Table S4 contains the crystallographic refinement data.

Synthesis and Characterization of $U_{1.23}Th_{4.77}$-Me_2BPDC-8. The green crystals of U_6-Me_2BPDC-8 (42 mg) were washed once with DMF and soaked in a 1.0 mL solution of 0.17 M $ThCl_4$ in DMF for 72 h at room temperature. After 72 h, the resulting crystals of $U_{1.23}Th_{4.77}$-Me_2BPDC-8 (U/Th-8) were collected by centrifugation and washed thoroughly three times with DMF. The PXRD pattern of $U_{1.23}Th_{4.77}$-Me_2BPDC-8 matches the simulated pattern. PXRD studies were used to confirm the crystallinity of the bulk material (Figure S14). IR (neat, cm^{-1}): 3389, 2930, 1648, 1587, 1543, 1497, 1409, 1383, 1254, 1206, 1140, 1093, 1062, 1007, 916, 863, 838, 777, 731, 721, and 659 (Figure S17). The XPS spectra are shown in Figures 3 and S13. The Tauc plot is shown in Figure S14b, and the estimated band gap for the prepared heterometallic MOF was found to be 2.5 eV.

Synthesis and Characterization of $U_{1.23}Th_{4.77}Co_3$-Me_2BPDC-8. The prepared $U_{1.23}Th_{4.77}$-Me_2BPDC-8 MOF (42.0 mg) was heated in a 0.25 M DMF solution (1.0 mL) of $Co(NO_3)_2{\cdot}6H_2O$ for 48 h in a preheated oven at 75 °C. As a result of such treatment, the sample changed color from gray to dark yellow-green. After the synthesis of $U_{1.23}Th_{4.77}$-Me_2BPDC-8, we employed a combination of PXRD to monitor the changes to the unit cell dimensions over 48 h, as well as XPS and Raman spectroscopies to determine the form of cobalt incorporated (Figures S14−S17). IR (neat, cm^{-1}): 3424, 2930, 1649, 1586, 1542, 1482, 1409, 1296, 1253, 1207, 1093, 1062, 1020, 1032, 1007, 912, 863, 815, 778, 734, and 659 (Figure S17). PXRD patterns were measured every 6 h over 48 h to probe changes in unit cell parameters as a function of time, as well as to monitor the incorporation process (Figure S14a). A single peak was observed (6.4°, 2θ) with a decrease in intensity as the metal-node extension proceeded, while another peak (5.1°, 2θ) shifted to higher angles. We modeled this change and calculated the diffraction intensity changes as a function of the occupancy of the cobalt ion. Indeed, our simulated diffraction pattern shows a decrease in peak intensity as a function of the amount of cobalt ion incorporated, a result comparable to that obtained experimentally (Figure S14c). To determine that the cobalt ion was incorporated as a metal node extension and not included as a guest in the form of either Co(II) or Co(III) oxides, we performed Raman and XPS measurements. In the Raman spectra, there was no detection of the presence of either Co(II) or Co(III) oxides (Figure S17). Furthermore, XPS data of the Co(2p) region supported the Raman data (Figure S15). The PXRD studies did not reveal the presence of crystalline cobalt oxides. Conductivity measurements of the heterometallic MOFs were performed in a home-built *in situ* pressed-pellet device. The metal ratio in the sample, thoroughly washed for 1 week using the Soxhlet washing procedure to ensure removal of any residual metal salts, was determined by ICP-MS analysis technique.

General Procedure To Study Structural Dynamism. The Th_6-Me_2BPDC-NO_3-10 and Th_6-Me_2BPDC-8 MOFs were soaked in 11 different solvents for 72 h during which the solvents were refreshed twice a day. Crystals suitable for single-crystal X-ray studies such as Th_6-Me_2BPDC-10-MeOH were analyzed. Detailed description of the data collection and refinement details of Th_6-Me_2BPDC-10-MeOH is given in the Supporting Information. Table S5 contains the crystallographic refinement data of Th_6-Me_2BPDC-10-MeOH. PXRD studies were used to monitor sample crystallinity (Figures S19, S22−S26).

General Linker Installation Procedure. Crystals of Th_6-Me_2BPDC-NO_3-10 or Th_6-Me_2BPDC-8 MOFs were soaked in 0.5 mL of the corresponding linker solution in DMF and heated at 75 °C in a preheated isothermal oven. The obtained crystals were collected by filtration and thoroughly washed with DMF using the Soxhlet extraction procedure. The samples were analyzed by single-crystal or powder X-ray diffraction. The linker installation was confirmed by ^1H NMR spectroscopy as described below.

Digestion Procedure. To study the linker composition of the synthesized MOFs by ^1H NMR spectroscopy, a mixture of 500 μL of DMSO-d_6 and 3 μL of concentrated HCl was added to 5 mg of thoroughly washed material (washing was done in DMF using the Soxhlet extraction method), followed by mild heating of the mixture to ensure complete dissolution of sample. The percent of linker installed was calculated based on linker ratios found in the ^1H NMR spectra of the digested samples. The amount of linker installed can be calculated from geometrical analysis of the parent MOF structure and length of the corresponding linker as shown by Zhou and co-workers.[52]

Synthesis and Characterization of Th_6-Me_2BPDC(Me_2TPDC)-12. Crystals of Th_6-Me_2BPDC-NO_3-10 (5.0 mg, 1.6 μmol) were heated in 0.5 mL of 15 mM H_2Me_2TPDC solution in DMF at 75 °C in a preheated isothermal oven for 24 h. This procedure resulted in the Th_6-Me_2BPDC-8 intermediate MOF as confirmed by single-crystal X-ray crystallography. The crystals of the Th_6-Me_2BPDC-8 intermediate were then heated for an additional 48 h in the presence of 0.5 mL of a 0.16 M H_2Me_2BPDC DMF solution. After that, the formed Th_6-Me_2BPDC(Me_2TPDC)-12 crystals were thoroughly washed with DMF to remove any residual linker. The crystals were suitable for single-crystal X-ray studies. Detailed description of the data collection and refinement details is given in the Supporting Information. Table S6 contains the crystallographic refinement data of the Th_6-Me_2BPDC-8 intermediate and Th_6-Me_2BPDC(Me_2TPDC)-12 crystals. PXRD studies were used to confirm the preserved framework integrity of the MOFs at every stage of the installation process (Figure S31). Based on ^1H NMR studies, the percentage of the installed linker is given in Table S9. The ^1H NMR spectrum is shown in Figure S34.

Attempts of H_2Me_2BPDC and H_2QPDC Installation into Th_6-Me_2BPDC-NO_3-10. Crystals of Th_6-Me_2BPDC-NO_3-10 (5.0 mg, 1.6 μmol) were heated in 0.5 mL of 0.16 M H_2Me_2BPDC solution in DMF at 75 °C in a preheated isothermal oven for 72 h. After that, crystals were thoroughly washed with DMF to remove any residual linker. Single-crystal X-ray studies of the crystals revealed no structural changes in the Th_6-Me_2BPDC-NO_3-10 structure. Based on the different orientation of adjacent metal nodes, the 12-coordinated MOF cannot be prepared through the installation of the H_2Me_2BPDC linker in the Th_6-Me_2BPDC-10 structure. Detailed description of the data collection and refinement details is given in the Supporting Information. Table S7 contains the crystallographic refinement data.

Crystals of Th_6-Me_2BPDC-NO_3-10 (5.0 mg, 1.6 μmol) were heated in 0.5 mL of 15 mM H_2QPDC solution in DMF at 75 °C in a preheated isothermal oven for 72 h. After heating, crystals were thoroughly washed with DMF to remove any residual linker. Single-crystal X-ray studies of the residual crystals revealed no structural changes in the Th_6-Me_2BPDC-NO_3-10 structure. Detailed description of the data collection and refinement details is in the Supporting Information. Table S7 contains the crystallographic refinement data.

Synthesis and Characterization of Th_6-Me_2BPDC(BDC)-10. Crystals of Th_6-Me_2BPDC-NO_3-10 (5.0 mg, 1.6 μmol) were heated in 0.5 mL of 0.16 M H_2BDC solution in DMF at 75 °C in a preheated isothermal oven for 24 h. After the installation process, the MOF was thoroughly washed with DMF to remove any residual linker. The crystals were unsuitable for single-crystal X-ray studies; however, PXRD studies were used to confirm the preserved framework integrity (Figure S31). Based on ^1H NMR studies, the percentage of the installed linker is given in Table S9, and the ^1H NMR spectrum is shown in Figure S35.

Synthesis and Characterization of Th_6-BPDC-10. Crystals of Th_6-Me_2BPDC-NO_3-10 (5.0 mg, 1.6 μmol) were heated in 0.5 mL of 16 mM H_2BPDC solution in DMF at 75 °C in a preheated isothermal oven for 48 h. After heating, crystals were thoroughly washed with DMF to remove any residual linker. Single-crystal X-ray studies of the obtained crystals demonstrate the Me_2BPDC^{2-}-to-$BPDC^{2-}$ linker replacement. Detailed description of the data collection and refinement details is given in the Supporting Information. Table S8 contains the crystallographic refinement data. PXRD studies were used to confirm the preserved framework integrity (Figure S32).

Synthesis and Characterization of Th_6-Me_2BPDC(Me_2TPDC)-10. Th_6-Me_2BPDC-8 (5.0 mg, 1.8 μmol) was heated in 0.5 mL of 15 mM H_2Me_2TPDC solution in DMF at 75 °C in a preheated isothermal oven for 72 h. After the installation process, the Th_6-Me_2BPDC(Me_2TPDC)-10 MOF was thoroughly washed with DMF to remove any residual linker. PXRD studies were used to confirm the preserved framework integrity of the MOFs at every stage of the installation process, as well as ensure the phase purity of the bulk sample (Figure S30). Based on ^{1}H NMR studies, the percentage of the installed linker is given in Table S9 and the spectrum is shown in Figure S37.

Synthesis and Characterization of Th_6-Me_2BPDC(Me_2BPDC)-10. Th_6-Me_2BPDC-8 (5.0 mg, 1.8 μmol) was heated in 0.5 mL of 0.16 M H_2Me_2BPDC solution in DMF at 75 °C in a preheated isothermal oven for 72 h. After the installation process, the Th_6-Me_2BPDC(Me_2BPDC)-10 MOF was thoroughly washed with DMF to remove any residual linker. PXRD studies were used to confirm the preserved framework integrity of the MOFs at every stage of the installation process, as well as ensure the phase purity of the bulk sample (Figure S30).

Synthesis and Characterization of Th_6-Me_2BPDC(BDC)-10. Th_6-Me_2BPDC-8 (5.0 mg, 1.8 μmol) was heated in 0.5 mL of 0.16 M H_2BDC solution in DMF at 75 °C in a preheated isothermal oven for 24 h. After the installation process, the Th_6-Me_2BPDC(BDC)-10 MOF was thoroughly washed with DMF to remove any residual linker. PXRD studies were used to confirm the preserved framework integrity as well as ensure the phase purity of the bulk MOF sample (Figure S31). Based on ^{1}H NMR studies, the percentage of the installed linker is given in Table S9. The ^{1}H NMR spectrum is shown in Figure S38.

Attempts of H_2QPDC Installation into Th_6-Me_2BPDC-8. Th_6-Me_2BPDC-8 (5.0 mg, 1.8 μmol) was heated in 0.5 mL of 15 mM H_2QPDC solution in DMF at 75 °C in a preheated isothermal oven for 72 h. After the installation process, the MOF was thoroughly washed with DMF to remove any residual linker. PXRD and spectroscopic studies did not indicate successful linker installation (Figure S31).

Physical Measurements. Single-crystal X-ray diffraction data were collected using a Bruker D8 QUEST diffractometer equipped with a PHOTON-100 CMOS area detector and an Incoatec microfocus source (Mo Kα radiation, λ = 0.71073 Å). Powder X-ray diffraction patterns were recorded on a Rigaku Miniflex II diffractometer with accelerating voltage and current of 30 kV and 15 mA, respectively. FTIR spectra were obtained on a PerkinElmer Spectrum 100. Raman spectra were measured using a Horiba XploraPLUS Raman spectrometer with diode laser (638 nm) and solid-state laser (473 nm) using a TE Air cooled CCD detector. NMR spectra were collected on Bruker Avance III-HD 300 and Bruker Avance III 400 MHz NMR spectrometers. The ^{1}H and ^{13}C NMR spectra were referenced to natural abundance ^{13}C signals and residual ^{1}H signals of deuterated solvents, respectively. Thermogravimetric analysis was performed on a SDT Q600 thermogravimetric analyzer using an alumina boat as a sample holder at a heating rate of 5 °C/min. ICP-MS analysis was conducted using a Finnigan ELEMENT XR double focusing magnetic sector field inductively coupled plasma-mass spectrometer (SF-ICP-MS) with Ir, Rh, or both as internal standards. A Micromist U-series nebulizer (0.2 mL/min, GE, Australia), quartz torch, and injector (Thermo Fisher Scientific, USA) were used for sample introduction. Sample gas flow was 1.08 mL/min, and the forwarding power was 1250 W. The samples were digested in Teflon vessels with nitric and hydrochloric acids and then heated at 180 °C for 4 h. X-ray photoelectron spectroscopy measurements were performed using a Kratos AXIS Ultra DLD XPS system with a monochromatic Al Kα source operated at 15 keV and 150 W and a hemispherical energy analyzer. Samples were placed in small powder pockets on the holder, and analysis was performed at a pressure below 1×10^{-9} mbar. High-resolution core level spectra were measured with a pass energy of 40 eV, and analysis of the data was carried out using XPSPEAK41 software. DR spectra were collected on an Ocean Optics JAZ spectrometer. An Ocean Optics ISP-REF integrating sphere was connected to the spectrometer using a 450 μm SMA fiber optic cable. Samples were loaded in an 8.0 mm quartz sample cell, which was referenced to an Ocean Optics WS-1 Spectralon standard. The conductivity measurements on MOF pressed pellets was performed using a source meter (Keithley Instruments GmbH, Germering, Germany, model 263) and an electrometer (Keithley Instruments GmbH, Germering, Germany, model 617).

Theoretical Calculations Methods. The DFT calculations were performed using the Vienna *ab initio* simulation package (VASP)[66,67] with plane wave basis sets. Projector-augmented wave (PAW)[68,69] pseudopotentials were employed, with the C $2s^22p^2$, H 1s, O $2s^22p^4$, Th $6s^27s^26p^66d^15f^1$, U $6s^27s^26p^66d^25f^2$, and Co $3d^84s^1$ treated explicitly. The geometries were optimized using the GGA-PBE[70] exchange correlation functionals. The van der Waals interactions were taken into account using the dispersion correction formula in the PBE-D3 functionals by Grimme et al.[71] with Becke–Johnson damping. In addition, an on-site Coulomb interaction was added to the uranium *f*-electrons and cobalt *d*-electrons within the DFT+U formalism[72] to attenuate the electron delocalization due to the self-interaction of electrons. Based on previous studies[73,74] a U-J = 4 eV was used for uranium. Although a U-J = 3 eV has been used for cobalt in previous literature,[75−77] this value underestimates the experimental band gap of Co containing systems in this work. Thus, a U-J = 4 eV was determined for Co to closely predict the conductivity measurements in this work. No DFT+U corrections are needed for Th, based on previous works[78,79] and also confirmed in this work. The plane-wave energy cutoff was set to 520 eV, and spin-polarized calculations were performed at the Γ-only k-point. Structural optimization was performed until the forces on each ion were less than 25 meV/Å, using 0.0001 eV as the energy tolerance criteria for the electronic step. Gaussian smearing with a width of 0.05 eV was applied to all optimizations. A conjugate-gradient algorithm[80,81] was used to relax all the ions. The calculations were performed on SBUs isolated in a cubic box of size 30 Å. The total and partial DOS were calculated by single point calculations following the geometry optimizations.

■ ASSOCIATED CONTENT

Supporting Information

The Supporting Information is available free of charge on the ACS Publications website at DOI: 10.1021/jacs.9b04737.

Additional experimental details, X-ray structure refinement data, PXRD patterns, TGA traces, FTIR, XPS, Tauc plots, ^{1}H NMR spectra and computational details (PDF)

Crystallographic information for Th_6-Me_2BPDC-NO_3-10, CCDC 1910421 (CIF)

Crystallographic information for Th_6-Me_2BPDC-8, CCDC 1910422 (CIF)

Crystallographic information for U_6-Me_2BPDC-TFA-10, CCDC 1910423 (CIF)

Crystallographic information for U_6-Me_2BPDC-8−1d-H_2O, CCDC 1910424 (CIF)

Crystallographic information for U_6-Me_2BPDC-8−4d-H_2O, CCDC 1910425 (CIF)

Crystallographic information for Th_6-Me_2BPDC-(Me_2TPDC)-12, CCDC 1910426 (CIF)

Crystallographic information for Th$_6$-Me$_2$BPDC-8-intermediate, CCDC 1910427 (CIF)

Crystallographic information for Th$_6$-Me$_2$BPDC-(“QPDC”)-10, CCDC 1910428 (CIF)

Crystallographic information for Th$_6$-Me$_2$BPDC-(“Me$_2$BPDC”)-10, CCDC 1910429 (CIF)

Crystallographic information for Th$_6$-Me$_2$BPDC-10-MeOH, CCDC 1910430 (CIF)

Crystallographic information for Th$_6$-BPDC-10, CCDC 1910431 (CIF)

Crystallographic information for Th$_6$-BPDC-12, CCDC 1910432 (CIF)

AUTHOR INFORMATION

Corresponding Author

*shustova@sc.edu

ORCID

Stavros G. Karakalos: 0000-0002-3428-5433
Brian A. Powell: 0000-0003-0423-0180
Hans-Conrad zur Loye: 0000-0001-7351-9098
Kyle S. Brinkman: 0000-0002-2219-1253
Natalia B. Shustova: 0000-0003-3952-1949

Notes

The authors declare no competing financial interest.

ACKNOWLEDGMENTS

This research was supported as part of the Center for Hierarchical Wasteform Materials (CHWM), an Energy Frontier Research Center funded by the U.S. Department of Energy, Office of Science under Award DE-SC0016574. N.B.S. acknowledges the support from the Sloan Research Fellowship provided by Alfred P. Sloan Foundation and Camille Dreyfus Teaching-Scholar Award provided by Henry and Camille Dreyfus Foundation.

REFERENCES

(1) Schrimpf, W.; Jiang, J.; Ji, Z.; Hirschle, P.; Lamb, D. C.; Yaghi, O. M.; Wuttke, S. Chemical Diversity in a Metal-Organic Framework Revealed by Fluorescence Lifetime Imaging. *Nat. Commun.* **2018**, *9*, 1647−1656.

(2) Wang, Y.; Liu, Z.; Li, Y.; Bai, Z.; Liu, W.; Wang, Y.; Xu, X.; Xiao, C.; Sheng, D.; Diwu, J.; Su, J.; Chai, Z.; Albrecht-Schmitt, T. E.; Shuao, W. Umbellate Distortions of the Uranyl Coordination Environment Result in a Stable and Porous Polycatenated Framework That Can Effectively Remove Cesium from Aqueous Solutions. *J. Am. Chem. Soc.* **2015**, *137*, 6144−6147.

(3) Dolgopolova, E. A.; Ejegbavwo, O. A.; Martin, C. R.; Smith, M. D.; Setyawan, W.; Karakalos, S. G.; Henager, C. H.; zur Loye, H.-C.; Shustova, N. B. Multifaceted Modularity: A Key for Stepwise Building of Hierarchical Complexity in Actinide Metal−Organic Frameworks. *J. Am. Chem. Soc.* **2017**, *139*, 16852−16861.

(4) Li, P.; Vermeulen, N. A.; Gong, X.; Malliakas, C. D.; Stoddart, J. F.; Hupp, J. T.; Farha, O. K. Design and Synthesis of a Water-Stable Anionic Uranium-Based Metal-Organic Framework (MOF) with Ultra Large Pores. *Angew. Chem., Int. Ed.* **2016**, *55*, 10358−10362.

(5) Furukawa, H.; Cordova, K. E.; O’Keeffe, M.; Yaghi, O. M. The Chemistry and Applications of Metal-Organic Frameworks. *Science* **2013**, *341*, 1230444−1230456.

(6) Li, P.; Wang, X.; Otake, K.; Lyu, J.; Hanna, S. L.; Islamoglu, T.; Farha, O. K. Synthetic Control of Thorium Polyoxo-Clusters in Metal−Organic Frameworks toward New Thorium-Based Materials. *ACS Appl. Nano Mater.* **2019**, *2*, 2260−2265.

(7) Kalmutzki, M. J.; Hanikel, N.; Yaghi, O. M. Secondary Building Units as the Turning Point in the Development of the Reticular Chemistry of MOFs. *Sci. Adv.* **2018**, *4*, 9180−9195.

(8) Kalaj, M.; Palomba, J. M.; Bentz, K. C.; Cohen, S. M. Multiple Functional Groups in UiO-66 Improve Chemical Warfare Agent Simulant Degradation. *Chem. Commun.* **2019**, *55*, 5367−5370.

(9) McGuirk, C.; Oktawiec, J.; Turkiewicz, A.; Taylor, M. K.; Long, J. R. Influence of Metal Substitution on the Pressure-Induced Phase Change in Flexible Zeolitic Imidazolate Frameworks. *J. Am. Chem. Soc.* **2018**, *140*, 15924−15933.

(10) Feng, M.; Zhang, P.; Zhou, H. C.; Sharma, V. K. Water-Stable Metal-Organic Frameworks for Aqueous Removal of Heavy Metals and Radionuclides: A Review. *Chemosphere* **2018**, *209*, 783−800.

(11) Ward, A. L.; Buckley, H. L.; Lukens, W. W.; Arnold, J. Synthesis and Characterization of Thorium(IV) and Uranium(IV) Corrole Complexes. *J. Am. Chem. Soc.* **2013**, *135*, 13965−13971.

(12) Li, Y. L.; Zeidman, B. D.; Hu, S. Y.; Henager, C. H.; Besmann, T. M.; Grandjean, A. A Physics-Based Mesoscale Phase-Field Model for Predicting the Uptake Kinetics of Radionuclides in Hierarchical Nuclear Wasteform Materials. *Comput. Mater. Sci.* **2019**, *159*, 103−109.

(13) Le Nedelec, T.; Charlot, A.; Calard, F.; Cuer, F.; Leydier, A.; Grandjean, A. Uranium Adsorption from Sulfuric Acid Media Using Silica Materials Functionalised with Amide and Phosphorous Ligands. *New J. Chem.* **2018**, *42*, 14300−14307.

(14) Yang, H.; Luo, L.; Wang, H.; Hu, D.; Lin, J.; Wang, X.; Wang, Y.; Wang, S.; Bu, X.; Feng, P.; Wu, T. Highly Selective and Rapid Uptake of Radionuclide Cesium Based on Robust Zeolitic Chalcogenide via Stepwise Ion-Exchange Strategy. *Chem. Mater.* **2016**, *28*, 8774−8780.

(15) Hendon, C. H.; Rieth, A. J.; Korzyński, M. D.; Dincă, M. Grand Challenges and Future Opportunities for Metal-Organic Frameworks. *ACS Cent. Sci.* **2017**, *3*, 554−563.

(16) Wang, H.; Lustig, W. P.; Li, J. Sensing and Capture of Toxic and Hazardous Gases and Vapors by Metal-Organic Frameworks. *Chem. Soc. Rev.* **2018**, *47*, 4729−4756.

(17) Yuan, S.; Feng, L.; Wang, K.; Pang, J.; Bosch, M.; Lollar, C.; Sun, Y.; Qin, J.; Yang, X.; Zhang, P.; Wang, Q.; Zou, L.; Zhang, Y.; Zhang, L.; Fang, Y.; Li, J.; Zhou, H.-C. Stable Metal-Organic Frameworks: Design, Synthesis, and Applications. *Adv. Mater.* **2018**, *30*, 1704303−1704337.

(18) Small, L. J.; Nenoff, T. M. Direct Electrical Detection of Iodine Gas by a Novel Metal−Organic-Framework-Based Sensor. *ACS Appl. Mater. Interfaces* **2017**, *9*, 44649−44655.

(19) Krause, S.; Bon, V.; Stoeck, U.; Senkovska, I.; Többens, D. M.; Wallacher, D.; Kaskel, S. A Stimuli-Responsive Zirconium Metal−Organic Framework Based on Supermolecular Design. *Angew. Chem., Int. Ed.* **2017**, *56*, 10676−10680.

(20) Carboni, M.; Abney, C. W.; Liu, S.; Lin, W. Highly Porous and Stable Metal−Organic Frameworks for Uranium Extraction. *Chem. Sci.* **2013**, *4*, 2396−2402.

(21) Li, P.; Vermeulen, N. A.; Malliakas, C. D.; Gómez-Gualdrón, D. A.; Howarth, A. J.; Mehdi, B. L.; Dohnalkova, A.; Browning, N. D.; O’Keeffe, M.; Farha, O. K. Bottom-up Construction of a Superstructure in a Porous Uranium-Organic Crystal. *Science* **2017**, *356*, 624−627.

(22) Su, J.; Chen, J. MOFs of Uranium and the Actinides. *Struct. Bonding (Berlin, Ger.)* **2014**, *163*, 265−296.

(23) Lollar, C. T.; Pang, J.; Qin, J.; Yuan, S.; Powell, J. A.; Zhou, H.-C. Thermodynamically Controlled Linker Installation in Flexible Zirconium Metal−Organic Frameworks. *Cryst. Growth Des.* **2019**, *19*, 2069−2073.

(24) Logan, M. W.; Adamson, J. D.; Le, D.; Uribe-Romo, F. J. Structural Stability of N-Alkyl-Functionalized Titanium Metal−Organic Frameworks in Aqueous and Humid Environments. *ACS Appl. Mater. Interfaces* **2017**, *9*, 44529−44533.

(25) Khabibullin, A.; Fullwood, E.; Kolbay, P.; Zharov, I. Reversible Assembly of Tunable Nanoporous Materials from “Hairy” Silica Nanoparticles. *ACS Appl. Mater. Interfaces* **2014**, *6*, 17306−17312.

(26) Pattengale, B.; SantaLucia, D. J.; Yang, S.; Hu, W.; Liu, C.; Zhang, X.; Berry, J. F.; Huang, J. Direct Observation of Node-to-Node Communication in Zeolitic Imidazolate Frameworks. *J. Am. Chem. Soc.* **2018**, *140*, 11573−11576.

(27) Xia, Z.; Poeppelmeier, K. R. Chemistry-Inspired Adaptable Framework Structures. *Acc. Chem. Res.* **2017**, *50*, 1222−1230.

(28) Zhang, Y.; Zhang, X.; Lyu, J.; Otake, K.-I.; Wang, X.; Redfern, L. R.; Malliakas, C. D.; Li, Z.; Islamoglu, T.; Wang, B.; Farha, O. K. A Flexible Metal-Organic Framework with 4-Connected Zr_6 Nodes. *J. Am. Chem. Soc.* **2018**, *140*, 11179−11183.

(29) Martin, N. P.; März, J.; Feuchter, H.; Duval, S.; Roussel, P.; Henry, N.; Ikeda-Ohno, A.; Loiseau, T.; Volkringer, C. Synthesis and Structural Characterization of the First Neptunium Based Metal-Organic Frameworks Incorporating {Np6O8} Hexanuclear Clusters. *Chem. Commun.* **2018**, *54*, 6979−6982.

(30) Cavka, J. H.; Jakobsen, S.; Olsbye, U.; Guillou, N.; Lamberti, C.; Bordiga, S.; Lillerud, K. P. A New Zirconium Inorganic Building Brick Forming Metal Organic Frameworks with Exceptional Stability. *J. Am. Chem. Soc.* **2008**, *130*, 13850−13851.

(31) Wang, H.; Dong, X.; Lin, J.; Teat, S. J.; Jensen, S.; Cure, J.; Alexandrov, E. V.; Xia, Q.; Tan, K.; Wang, Q.; Olson, D. H.; Proserpio, D. M.; Chabal, Y. J.; Thonhauser, T.; Sun, J.; Han, Y.; Li, J. Topologically Guided Tuning of Zr-MOF Pore Structures for Highly Selective Separation of C6 Alkane Isomers. *Nat. Commun.* **2018**, *9*, 1745−1755.

(32) Bueken, B.; Vermoortele, F.; Cliffe, M. J.; Wharmby, M. T.; Foucher, D.; Wieme, J.; Vanduyfhuys, L.; Martineau, C.; Stock, N.; Taulelle, F.; Van Speybroeck, V.; Goodwin, A. L.; De Vos, D. A Breathing Zirconium Metal-Organic Framework with Reversible Loss of Crystallinity by Correlated Nanodomain Formation. *Chem. - Eur. J.* **2016**, *22*, 3264−3267.

(33) Deria, P.; Gómez-Gualdrón, D. A.; Bury, W.; Schaef, H. T.; Wang, T. C.; Thallapally, P. K.; Sarjeant, A. A.; Snurr, R. Q.; Hupp, J. T.; Farha, O. K. Ultraporous, Water Stable, and Breathing Zirconium-Based Metal-Organic Frameworks with Ftw Topology. *J. Am. Chem. Soc.* **2015**, *137*, 13183−13190.

(34) Furukawa, H.; Gándara, F.; Zhang, Y.-B.; Jiang, J.; Queen, W. L.; Hudson, M. R.; Yaghi, O. M. Water Adsorption in Porous Metal−Organic Frameworks and Related Materials. *J. Am. Chem. Soc.* **2014**, *136*, 4369−4381.

(35) Souza, B. E.; Rudić, S.; Titov, K.; Babal, A. S.; Taylor, J. D.; Tan, J.-C. Guest−Host Interactions of Nanoconfined Anti-Cancer Drug in Metal−Organic Framework Exposed by Terahertz Dynamics. *Chem. Commun.* **2019**, *55*, 3868−3871.

(36) Devic, T.; Horcajada, P.; Serre, C.; Salles, F.; Maurin, G.; Moulin, B.; Heurtaux, D.; Clet, G.; Vimont, A.; Grenéche, J. M.; Le Ouay, B.; Moreau, F.; Magnier, E.; Filinchuk, Y.; Marrot, J.; Lavalley, J.; Daturi, M.; Férey, G. Functionalization in Flexible Porous Solids: Effects on the Pore Opening and the Host-Guest Interactions. *J. Am. Chem. Soc.* **2010**, *132*, 1127−1136.

(37) Lee, S.; Bürgi, H. B.; Alshmimri, S. A.; Yaghi, O. M. Impact of Disordered Guest-Framework Interactions on the Crystallography of Metal-Organic Frameworks. *J. Am. Chem. Soc.* **2018**, *140*, 8958−8964.

(38) Bhunia, M. K.; Hughes, J. T.; Fettinger, J. C.; Navrotsky, A. Thermochemistry of Paddle Wheel MOFs: Cu-HKUST-1 and Zn-HKUST-1. *Langmuir* **2013**, *29*, 8140−8145.

(39) Joback, K. G.; Reid, R. C. Estimation of Pure-Component Properties from Group-Contributions. *Chem. Eng. Commun.* **1987**, *57*, 233−243.

(40) OECD/NEA (2008), *Chemical Thermodynamics of Thorium*, Chemical Thermodynamics, OECD Publishing, Paris.

(41) Robie, R. A.; Hemingway, B. S. *Thermodynamic Properties of Minerals and Related Substances at 298.15 K and 1 bar (105 Pascals) Pressure and at Higher Temperatures*; Washington, 1995.

(42) Vasil'eva, T. F.; Zhil'tsova, E. N.; Vvedenskii, A. A. Enthalpies of Combustion of NN-Dimethylformamide and NN-Dimethylacetamide. *Russ. J. Phys. Chem. (Engl. Transl.)* **1972**, *46*, 315.

(43) Hughes, J. T.; Navrotsky, A. MOF-5: Enthalpy of Formation and Energy Landscape of Porous Materials. *J. Am. Chem. Soc.* **2011**, *133*, 9184−9187.

(44) Akimbekov, Z.; Wu, D.; Brozek, C. K.; Dincă, M.; Navrotsky, A. Thermodynamics of Solvent Interaction with the Metal−Organic Framework MOF-5. *Phys. Chem. Chem. Phys.* **2016**, *18*, 1158−1162.

(45) Bureekaew, S.; Amirjalayer, S.; Schmid, R. Orbital Directing Effects in Copper and Zinc Based Paddle-Wheel Metal Organic Frameworks: The Origin of Flexibility. *J. Mater. Chem.* **2012**, *22*, 10249−10254.

(46) Hughes, J. T.; Bennett, T. D.; Cheetham, A. K.; Navrotsky, A. Thermochemistry of Zeolitic Imidazolate Frameworks of Varying Porosity. *J. Am. Chem. Soc.* **2013**, *135*, 598−601.

(47) Yuan, S.; Chen, Y.-P.; Qin, J.-S.; Lu, W.; Wang, X.; Zhang, Q.; Bosch, M.; Liu, T.-F.; Lian, X.; Zhou, H.-C. Cooperative Cluster Metalation and Ligand Migration in Zirconium Metal-Organic Frameworks. *Angew. Chem., Int. Ed.* **2015**, *54*, 14696−14700.

(48) Falaise, C.; Delille, J.; Volkringer, C.; Vezin, H.; Rabu, P.; Loiseau, T. Series of Hydrated Heterometallic Uranyl-Cobalt(II) Coordination Polymers with Aromatic Polycarboxylate Ligands: Formation of U═O−Co Bonding upon Dehydration Process. *Inorg. Chem.* **2016**, *55*, 10453−10466.

(49) Schneemann, A.; Bon, V.; Schwedler, I.; Senkovska, I.; Kaskel, S.; Fischer, R. A. Flexible Metal-Organic Frameworks. *Chem. Soc. Rev.* **2014**, *43*, 6062−6096.

(50) Chen, C. X.; Wei, Z.; Jiang, J. J.; Fan, Y. Z.; Zheng, S. P.; Cao, C. C.; Li, Y. H.; Fenske, D.; Su, C. Y. Precise Modulation of the Breathing Behavior and Pore Surface in Zr-MOFs by Reversible Post-Synthetic Variable-Spacer Installation to Fine-Tune the Expansion Magnitude and Sorption Properties. *Angew. Chem., Int. Ed.* **2016**, *55*, 9932−9936.

(51) Schaate, A.; Roy, P.; Godt, A.; Lippke, J.; Waltz, F.; Wiebcke, M.; Behrens, P. Modulated Synthesis of Zr-Based Metal-Organic Frameworks: From Nano to Single Crystals. *Chem. - Eur. J.* **2011**, *17*, 6643−6651.

(52) Yuan, S.; Lu, W.; Chen, Y.-P.; Zhang, Q.; Liu, T.-F.; Feng, D.; Wang, X.; Qin, J.-S.; Zhou, H.-C. Sequential Linker Installation: Precise Placement of Functional Groups in Multivariate Metal-Organic Frameworks. *J. Am. Chem. Soc.* **2015**, *137*, 3177−3180.

(53) Halder, A.; Ghoshal, D. Structure and Properties of Dynamic Metal-Organic Frameworks: A Brief Accounts of Crystalline-to-Crystalline and Crystalline-to-Amorphous Transformations. *CrystEngComm* **2018**, *20*, 1322−1345.

(54) Helal, A.; Yamani, Z. H.; Cordova, K. E.; Yaghi, O. M. Multivariate Metal-Organic Frameworks. *Natl. Sci. Rev.* **2017**, *4*, 296−298.

(55) Zhang, Y. B.; Furukawa, H.; Ko, N.; Nie, W.; Park, H. J.; Okajima, S.; Cordova, K. E.; Deng, H.; Kim, J.; Yaghi, O. M. Introduction of Functionality, Selection of Topology, and Enhancement of Gas Adsorption in Multivariate Metal-Organic Framework-177. *J. Am. Chem. Soc.* **2015**, *137*, 2641−2650.

(56) Chen, W.; Zhang, P.; Zhou, H.-C.; Drake, H. F.; Zhang, L.; Yuan, S.; Sokaras, D.; Day, G. S.; Feng, L.; Elumalai, P.; Madrahimov, S. T.; Sun, D.; Qun, J.-S.; Garcia-Esparza, A. T. Exposed Equatorial Positions of Metal Centers via Sequential Ligand Elimination and Installation in MOFs. *J. Am. Chem. Soc.* **2018**, *140*, 10814−10819.

(57) Yuan, S.; Chen, Y. P.; Qin, J. S.; Lu, W.; Zou, L.; Zhang, Q.; Wang, X.; Sun, X.; Zhou, H. C. Linker Installation: Engineering Pore Environment with Precisely Placed Functionalities in Zirconium MOFs. *J. Am. Chem. Soc.* **2016**, *138*, 8912−8919.

(58) Cao, C. C.; Chen, C. X.; Wei, Z. W.; Qiu, Q. F.; Zhu, N. X.; Xiong, Y. Y.; Jiang, J. J.; Wang, D.; Su, C. Y. Catalysis through Dynamic Spacer Installation of Multivariate Functionalities in Metal-Organic Frameworks. *J. Am. Chem. Soc.* **2019**, *141*, 2589−2593.

(59) Luo, T. Y.; Liu, C.; Gan, X. Y.; Muldoon, P. F.; Diemler, N. A.; Millstone, J. E.; Rosi, N. L. Multivariate Stratified Metal-Organic Frameworks: Diversification Using Domain Building Blocks. *J. Am. Chem. Soc.* **2019**, *141*, 2161−2168.

(60) Zur Loye, H. C.; Besmann, T.; Amoroso, J.; Brinkman, K.; Grandjean, A.; Henager, C. H.; Hu, S.; Misture, S. T.; Phillpot, S. R.; Shustova, N. B.; Wang, H.; Koch, R.; Morrison, G.; Dolgopolova, E. Hierarchical Materials as Tailored Nuclear Waste Forms: A Perspective. *Chem. Mater.* **2018**, *30*, 4475−4488.

(61) Hu, P.; Yin, L.; Kirchon, A.; Li, J.; Li, B.; Wang, Z.; Ouyang, Z.; Zhang, T.; Zhou, H.-C. Magnetic Metal−Organic Framework Exhibiting Quick and Selective Solvatochromic Behavior along with Reversible Crystal-to-Amorphous-to-Crystal Transformation. *Inorg. Chem.* **2018**, *57*, 7006−7014.

(62) Deng, M.; Pan, Y.; Zhu, J.; Chen, Z.; Sun, Z.; Sun, J.; Ling, Y.; Zhou, Y.; Feng, P. Cation-Exchange Approach to Tuning the Flexibility of a Metal−Organic Framework for Gated Adsorption. *Inorg. Chem.* **2017**, *56*, 5069−5075.

(63) Burrows, A. D.; Frost, C. G.; Mahon, M. F.; Richardson, C. Sulfur-Tagged Metal-Organic Frameworks and Their Post-Synthetic Oxidation. *Chem. Commun.* **2009**, *0*, 4218−4220.

(64) Bowen, A. M.; Jones, M. W.; Lovett, J. E.; Gaule, T. G.; McPherson, M. J.; Dilworth, J. R.; Timmel, C. R.; Harmer, J. R. Exploiting Orientation-Selective DEER: Determining Molecular Structure in Systems Containing Cu(II) Centres. *Phys. Chem. Chem. Phys.* **2016**, *18*, 5981−5994.

(65) Hylland, K.; Øien-Ødegaard, S.; Lillerud, K.; Tilset, M. Efficient, Scalable Syntheses of Linker Molecules for Metal-Organic Frameworks. *Synlett* **2015**, *26*, 1480−1485.

(66) Kresse, G.; Hafner, J. Ab Initio Molecular Dynamics for Liquid Metals. *Phys. Rev. B: Condens. Matter Mater. Phys.* **1993**, *47*, 558−561.

(67) Kresse, G.; Furthmüller, J. Efficient Iterative Schemes for Ab Initio Total-Energy Calculations Using a Plane-Wave Basis Set. *Phys. Rev. B: Condens. Matter Mater. Phys.* **1996**, *54*, 11169−11186.

(68) Blöchl, P. E. Projector Augmented-Wave Method. *Phys. Rev. B: Condens. Matter Mater. Phys.* **1994**, *50*, 17953−17979.

(69) Kresse, G.; Joubert, D. From Ultrasoft Pseudopotentials to the Projector Augmented-Wave Method. *Phys. Rev. B: Condens. Matter Mater. Phys.* **1999**, *59*, 1758−1775.

(70) Perdew, J. P.; Burke, K.; Ernzerhof, M. Generalized Gradient Approximation Made Simple. *Phys. Rev. Lett.* **1996**, *77*, 3865−3868.

(71) Grimme, S.; Antony, J.; Ehrlich, S.; Krieg, H. A Consistent and Accurate Ab Initio Parametrization of Density Functional Dispersion Correction (DFT-D) for the 94 Elements H-Pu. *J. Chem. Phys.* **2010**, *132*, 154104−154122.

(72) Dudarev, S. L.; Botton, G. A.; Savrasov, S. Y.; Humphreys, C. J.; Sutton, A. P. Electron-Energy-Loss Spectra and the Structural Stability of Nickel Oxide: An LSDA+U Study. *Phys. Rev. B: Condens. Matter Mater. Phys.* **1998**, *57*, 1505−1509.

(73) Dorado, B.; Amadon, B.; Freyss, M.; Bertolus, M. DFT+U Calculations of the Ground State and Metastable States of Uranium Dioxide. *Phys. Rev. B: Condens. Matter Mater. Phys.* **2009**, *79*, 235125−235132.

(74) Dudarev, S. L.; Castell, M. R.; Botton, G. A.; Savrasov, S. Y.; Muggelberg, C.; Briggs, G. A. D.; Sutton, A. P.; Goddard, D. T. Understanding STM Images and EELS Spectra of Oxides with Strongly Correlated Electrons: A Comparison of Nickel and Uranium Oxides. *Micron* **2000**, *31*, 363−372.

(75) Ritzmann, A. M.; Pavone, M.; Muñoz-García, A. B.; Keith, J. A.; Carter, E. A. Ab Initio DFT+U Analysis of Oxygen Transport in LaCoO 3: The Effect of Co 3+ Magnetic States. *J. Mater. Chem. A* **2014**, *2*, 8060−8074.

(76) Zhang, S.; Han, N.; Tan, X. Density Functional Theory Calculations of Atomic, Electronic and Thermodynamic Properties of Cubic $LaCoO_3$ and $La_{1-x}Sr_xCoO_3$ Surfaces. *RSC Adv.* **2015**, *5*, 760−769.

(77) Olsson, E.; Aparicio-Anglès, X.; De Leeuw, N. H. Ab Initio Study of Vacancy Formation in Cubic LaMnO3 and SmCoO3 as Cathode Materials in Solid Oxide Fuel Cells. *J. Chem. Phys.* **2016**, *145*, 014703−014712.

(78) Shields, A. E.; Santos-Carballal, D.; De Leeuw, N. H. A Density Functional Theory Study of Uranium-Doped Thoria and Uranium Adatoms on the Major Surfaces of Thorium Dioxide. *J. Nucl. Mater.* **2016**, *473*, 99−111.

(79) Pegg, J. T.; Aparicio-Anglès, X.; Storr, M.; de Leeuw, N. H. DFT+U Study of the Structures and Properties of the Actinide Dioxides. *J. Nucl. Mater.* **2017**, *492*, 269−278.

(80) Bylander, D. M.; Kleinman, L.; Lee, S. Self-Consistent Calculations of the Energy Bands and Bonding Properties of B 12 C 3. *Phys. Rev. B: Condens. Matter Mater. Phys.* **1990**, *42*, 1394−1403.

(81) Teter, M. P.; Payne, M. C.; Allan, D. C. Solution of Schrödinger's Equation for Large Systems. *Phys. Rev. B: Condens. Matter Mater. Phys.* **1989**, *40*, 12255−12263.